GEOPHYSICS, VOL. 76, NO. 3 (MAY-JUNE 2011); P. S131–S141, 11 FIGS.
10.1190/1.3560519

Wide-azimuth angle gathers for wave-equation migration

Paul Sava[1] and Ioan Vlad[2]

ABSTRACT

Extended common-image-point (CIP) gathers contain all of the necessary information for decomposition of reflectivity as a function of the reflection and azimuth angles at selected locations in the subsurface. This decomposition operates after the imaging condition applied to wavefields reconstructed by any type of wide-azimuth migration method, e.g., using downward continuation or time reversal. The reflection and azimuth angles are derived from the extended images using analytic relations between the space-lag and time-lag extensions. The transformation amounts to a linear Radon transform applied to the CIPs obtained after applying the extended imaging condition. If information about the reflector dip is available at the CIP locations, then only two components of the space-lag vectors are required, thus reducing computational cost and increasing the affordability of the method. Applications of this method include the study of subsurface illumination in areas of complex geology where ray-based methods are not usable and the study of amplitude variation with reflection and azimuth angles if the subsurface illumination is sufficiently dense. Migration velocity analysis could also be implemented in the angle domain, although an equivalent implementation in the extended domain is less costly and more effective.

INTRODUCTION

In regions characterized by complex subsurface structure, wave-equation depth migration is a powerful tool for accurately imaging the earth's interior. The quality of the final image greatly depends on the quality of the velocity model and on the quality of the technique used for wavefield reconstruction in the subsurface (Gray et al., 2001).

However, structural imaging is not the only objective of wave-equation imaging. It is often desirable to construct images depicting reflectivity as a function of reflection angles. Such images not only highlight the subsurface illumination patterns but could be used for image postprocessing for amplitude variation with angle (AVA) analysis. Furthermore, angle-domain images can be used for tomographic velocity updates.

Angle gathers can be produced using ray methods (Xu et al., 1998; Brandsberg-Dahl et al., 2003) or wavefield methods (de Bruin et al., 1990; Mosher et al., 1997; Prucha et al., 1999; Rickett and Sava, 2002; Xie and Wu, 2002; Sava and Fomel, 2003; Biondi and Symes, 2004; Wu and Chen, 2006). Gathers constructed with these methods have similar characteristics because they describe the reflectivity as a function of incidence angles at the reflector. However, as indicated by Stolk and Symes (2004), even in perfectly known but strongly refracting media, angle gathers are damaged by undersampling data on the surface, regardless of the method used for their construction. In this paper, we address the problem of wavefield-based angle decomposition.

Angle decomposition can be applied before or after the application of an imaging condition. The two classes of methods differ by the objects used to study the angle-dependent illumination of subsurface geology. The methods operating before the imaging condition decompose the extrapolated wavefields from the source and receivers (de Bruin et al., 1990; Mosher et al., 1997; Prucha et al., 1999; Wu and Chen, 2006). This type of decomposition is costly because it operates on individual wavefields characterized by complex multipathing. In contrast, the methods operating after the imaging condition decompose the images themselves, which are represented as a function of space and additional parameters, typically referred to as extensions (Rickett and Sava, 2002; Sava and Fomel, 2003, 2006; Sava and Vasconcelos, 2011). In the end, the various classes of methods lead to similar representations of the angle-dependent reflectivity represented by the so-called

Manuscript received by the Editor 19 September 2010; revised manuscript received 16 December 2010; published online 16 May 2011.
[1]Colorado School of Mines, Department of Geophysics, Center for Wave Phenomena, Golden, Colorado, U.S.A. E-mail: psava@mines.edu.
[2]Formerly Statoil; presently Fusion Petroleum Technologies, Houston, Texas, U.S.A. E-mail: nvlad@fusiongeo.com.
© 2011 Society of Exploration Geophysicists. All rights reserved.

Downloaded 16 May 2011 to 138.67.179.205. Redistribution subject to SEG license or copyright; see Terms of Use at http://segdl.org/

scattering matrix. The main differences lie in the complexity of the decomposition and in the cost required to achieve this result. Here, our work focuses on angle decomposition of extended images.

Conventionally, angle-domain imaging uses common-image gathers (CIGs) describing the reflectivity as a function of reflection angles and a space axis, typically the depth axis. An alternative way of constructing angle-dependent reflectivity is based on common-image-point (CIP) gathers selected at various positions in the subsurface. As pointed out by Sava and Vasconcelos (2011), CIP gathers are advantageous because they sample the image at the most relevant locations (along the main reflectors), they avoid computations at locations that are not useful for further analysis (inside salt bodies), they can have higher density at locations where the structure is more complex and lower density in areas of poor illumination, and they avoid the depth bias typical for gathers constructed as a function of the depth axis. Throughout our paper, we focus on angle decomposition using extended CIP gathers.

A recent development in wave-equation imaging is the use of wide-azimuth data (Clarke et al., 2006; Michell et al., 2006; Regone, 2006). Imaging with such data poses additional challenges for angle-domain imaging, mainly arising from the larger data-set size and the interpretation difficulty of data of higher dimensionality. Several techniques have been proposed for wide-azimuth angle decomposition, including ray-based methods (Koren et al., 2008) and wavefield methods using wavefield decomposition before imaging (Biondi and Tisserant, 2004; Zhu and Wu, 2010) or after imaging (Sava and Fomel, 2005). Here, we complete the set of techniques available for angle-gather construction by describing an algorithm applicable to extended CIP gathers.

IMAGING CONDITIONS

Conventional seismic imaging is based on the concept of single scattering. Under this assumption, waves propagate from seismic sources, interact with discontinuities, and return to the surface as reflected seismic waves. We commonly speak about a source wavefield, originating at the seismic source and propagating in the medium prior to any interaction with discontinuities, and a receiver wavefield, originating at discontinuities and propagating in the medium to the receivers (Berkhout, 1982; Claerbout, 1985). The two wavefields coincide kinematically at discontinuities.

We can formulate imaging as a process involving two steps: wavefield reconstruction and the imaging condition. The key elements in this imaging procedure are the source wavefield W_s and the receiver wavefield W_r, which are 4D objects as a function of space $\mathbf{x}=\{x,y,z\}$ and time t or as a function of space and frequency ω. For imaging, we need to analyze if the wavefields match kinematically in time and then extract the reflectivity information using an imaging condition operating along the space and time axes.

A conventional crosscorrelation imaging condition based on the reconstructed wavefields can be formulated in the time or frequency domain as the zero lag of the crosscorrelation between the source and receiver wavefields (Claerbout, 1985):

$$R(\mathbf{x})=\sum_{\text{shots}}\sum_{t}W_s(\mathbf{x},t)W_r(\mathbf{x},t) \quad (1)$$

$$=\sum_{\text{shots}}\sum_{\omega}\overline{W_s(\mathbf{x},\omega)}W_r(\mathbf{x},\omega), \quad (2)$$

where R represents the migrated image and the overbar represents complex conjugation. This operation exploits the fact that portions of the source and receiver wavefields match kinematically at subsurface positions where discontinuities occur. Alternative imaging conditions use deconvolution of the source and receiver wavefields, but we do not elaborate on this subject because the differences between crosscorrelation and deconvolution are not central for this paper.

An extended imaging condition preserves in the output image certain acquisition (e.g., source or receiver coordinates) or illumination (e.g., reflection angle) parameters (Clayton and Stolt, 1981; Claerbout, 1985; Stolt and Weglein, 1985; Weglein and Stolt, 1999). In shot-record migration, the source and receiver wavefields are reconstructed on the same computational grid at all locations in space and all times or frequencies. Therefore, no a priori wavefield separation can be transferred to the output image. In this situation, the separation can be constructed by correlating the wavefields from symmetric locations relative to the image point, measured in space (Rickett and Sava, 2002; Sava and Fomel, 2005) or in time (Sava and Fomel, 2006). This separation essentially represents local crosscorrelation lags between the source and receiver wavefields. Thus, an extended crosscorrelation imaging condition defines the image as a function of space and crosscorrelation lags in space and time. This imaging condition can also be formulated in the time and frequency domains (Sava and Vasconcelos, 2011):

$$R(\mathbf{x},\boldsymbol{\lambda},\tau)=\sum_{\text{shots}}\sum_{t}W_s(\mathbf{x}-\boldsymbol{\lambda},t-\tau)W_r(\mathbf{x}+\boldsymbol{\lambda},t+\tau) \quad (3)$$

$$=\sum_{\text{shots}}\sum_{\omega}e^{2i\omega\tau}\overline{W_s(\mathbf{x}-\boldsymbol{\lambda},\omega)}W_r(\mathbf{x}+\boldsymbol{\lambda},\omega). \quad (4)$$

Equations 1 and 2 represent a special case of equations 3 and 4 for $\boldsymbol{\lambda}=0$ and $\tau=0$. Assuming that all errors accumulated in the incorrectly reconstructed wavefields result from the velocity model, the extended images could be used for velocity model-building by exploiting semblance properties emphasized by the space lags (Biondi and Sava, 1999; Shen et al., 2003; Sava and Biondi, 2004a, 2004b) and focusing properties emphasized by the time lag (Faye and Jeannot, 1986; MacKay and Abma, 1992, 1993; Nemeth, 1995, 1996). Furthermore, these extensions can be converted to reflection angles (Weglein and Stolt, 1999; Sava and Fomel, 2003, 2006), thus enabling AVA analysis for images constructed in complex areas using wavefield-based imaging.

Typically, angle decomposition with extended images uses CIGs, i.e., representations of (a subset of) the extensions as a function of a space axis — typically, the depth axis. As pointed out by Sava and Vasconcelos (2011), this approach suffers from major drawbacks. CIGs are appropriate for nearly horizontal structures, but they are computationally wasteful because they

Downloaded 16 May 2011 to 138.67.179.205. Redistribution subject to SEG license or copyright; see Terms of Use at http://segdl.org/

require unnecessary calculations, e.g., inside massive salt bodies. In contrast, the CIP gathers advocated by Sava and Vasconcelos (2011) are constructed at selected points in the image, thus eliminating unnecessary calculations. They can also accommodate arbitrary orientations of the reflectors.

In this paper, we use extended CIP gathers to extract angle-dependent reflectivity at individual points in the image. Our method is appropriate for 3D wide-azimuth wave-equation imaging. The problem we are solving is how to decompose extended CIP gathers as a function of azimuth ϕ and reflection θ angles at selected points in the image. In general, the input for such decomposition are gathers in the $\{\boldsymbol{\lambda}, \tau\}$ domain and the output are gathers in the $\{\phi, \theta, \tau\}$ domain:

$$R(\boldsymbol{\lambda}, \tau) \Rightarrow R(\phi, \theta, \tau). \tag{5}$$

We address a special case of this decomposition that is appropriate for imaging with correct velocity. In this case, all of the energy in the output CIP gather concentrates at $\tau = 0$, so we can focus our attention on a particular case of the decomposition that does not preserve the time-lag variable in the output: $R(\boldsymbol{\lambda}, \tau) \Rightarrow R(\phi, \theta)$. We omit the dependence of the extended images on space $\mathbf{x}$ to highlight the fact that the decomposition can be performed independently at various points in the image. The topic of angle decomposition when the gathers are constructed with incorrect velocity remains outside the scope of this paper. However, the angle decomposition in such a situation is unnecessary because semblance optimization can be implemented based directly on the image extensions (Shen and Symes, 2008; Symes, 2008).

All of the information necessary for this decomposition is available after wave-equation migration, regardless of its implementation, e.g., by depth or time extrapolation. A prerequisite for this decomposition is the moveout function characterizing individual shots. Moveout information can be used for angle decomposition, as we illustrate in the following simple and complex synthetic examples.

MOVEOUT FUNCTION

In this section, we derive the formula for the moveout function characterizing reflections in the extended $\{\boldsymbol{\lambda}, \tau\}$ domain. The purpose of this derivation is to find a procedure for angle decomposition, i.e., a representation of reflectivity as a function of reflection and azimuth angles.

An implicit assumption made by all methods of angle decomposition is that we can describe the reflection process by locally planar objects. Such methods assume that (locally) the reflector is a plane and that the incident and reflected wavefields are also (locally) planar. Only with these assumptions can we define vectors in between which we measure angles such as incidence and reflection, as well as the azimuth angle of the reflection plane. Our method uses this assumption explicitly. However, we do not assume that the wavefronts are planar. Instead, we consider each (complex) wavefront as a superposition of planes with different orientations. In this section, we discuss how each one of these planes would behave during the extended imaging and angle decomposition, confirming that our method applies equally well for simple and complex wavefields characterized by multipathing.

We define five unit vectors to describe the reflection geometry and the conventional and extended imaging conditions: $\mathbf{n}$ is aligned with the reflector normal; $\mathbf{a}$ represents the projection of the azimuth vector $\mathbf{v}$ in the reflector plane; $\mathbf{n}_s$ is orthogonal to the source wavefront; $\mathbf{n}_r$ is orthogonal to the receiver wavefront; and $\mathbf{q}$ is at the intersection of the reflection plane and the reflector plane. By construction, $\mathbf{n}$, $\mathbf{n}_s$, $\mathbf{n}_r$, and $\mathbf{q}$ are coplanar; $\mathbf{n}$ and $\mathbf{q}$ are orthogonal (Figure 1).

With these definitions, the (planar) source and receiver wavefields are given by the expressions

$$\mathbf{n}_s \cdot \mathbf{x} = V t_s, \tag{6}$$

$$\mathbf{n}_r \cdot \mathbf{x} = V t_r. \tag{7}$$

Here, $\mathbf{x}$ are space coordinates, t_s and t_r are times defining the planes under consideration, and V represents velocity. Equations 6 and 7 define the conventional imaging condition given by equations 1 and 2. This condition states that an image is formed when the source and receiver wavefields are time coincident at reflection points. In equations 6 and 7, we explicitly impose the condition that the source and receiver planes and the reflector plane intersect at the image point.

Similarly, we can rewrite the extended imaging condition using the planar approximation of the source and receiver wavefields using the expressions

$$\mathbf{n}_s \cdot (\mathbf{x} - \boldsymbol{\lambda}) = V(t_s - \tau), \tag{8}$$

$$\mathbf{n}_r \cdot (\mathbf{x} + \boldsymbol{\lambda}) = V(t_r + \tau). \tag{9}$$

As discussed, $\boldsymbol{\lambda}$ and τ are space and time lags, and V represents the local velocity at the image point, assumed to be constant in the immediate vicinity of this point. This assumption is justified by the need to operate with planar objects. With this construction, the source and receiver planes are shifted relative to one another by equal quantities in the positive and negative directions in space and time (equations 3 and 4).

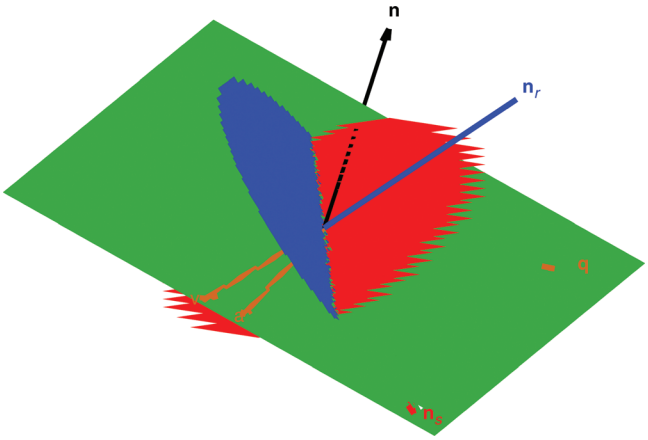


Figure 1. The reflector plane of normal $\mathbf{n}$, together with the source and receiver planes of normals $\mathbf{n}_s$ and $\mathbf{n}_r$, respectively. The figure represents the source/receiver planes in their original position, i.e., as obtained by wavefield reconstruction.

Downloaded 16 May 2011 to 138.67.179.205. Redistribution subject to SEG license or copyright; see Terms of Use at http://segdl.org/

We can eliminate $\mathbf{x}$ by substituting equation 6 into equation 8 and substituting equation 7 into equation 9:

$$\mathbf{n}_s \cdot \boldsymbol{\lambda} = V\tau, \tag{10}$$

$$\mathbf{n}_r \cdot \boldsymbol{\lambda} = V\tau. \tag{11}$$

Furthermore, we can rearrange the system given by equations 10 and 11 by sum and difference of the equations:

$$(\mathbf{n}_s + \mathbf{n}_r) \cdot \boldsymbol{\lambda} = 2V\tau, \tag{12}$$

$$(\mathbf{n}_s - \mathbf{n}_r) \cdot \boldsymbol{\lambda} = 0. \tag{13}$$

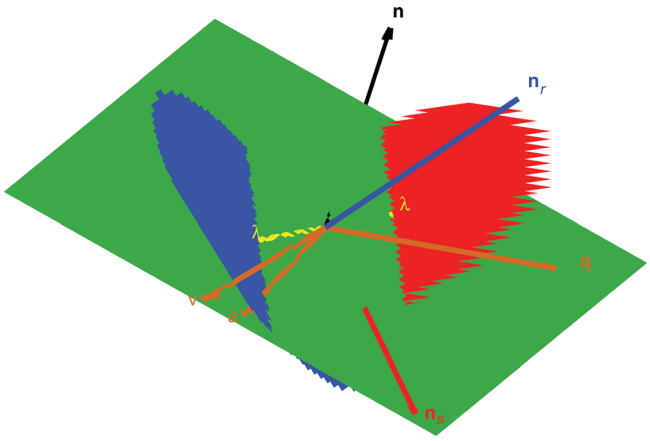


Figure 2. The reflector plane of normal $\mathbf{n}$, together with the source and receiver planes of normals $\mathbf{n}_s$ and $\mathbf{n}_r$, respectively. The figure represents the source/receiver planes displaced with the space lag $\boldsymbol{\lambda}$ constrained in the reflector plane.

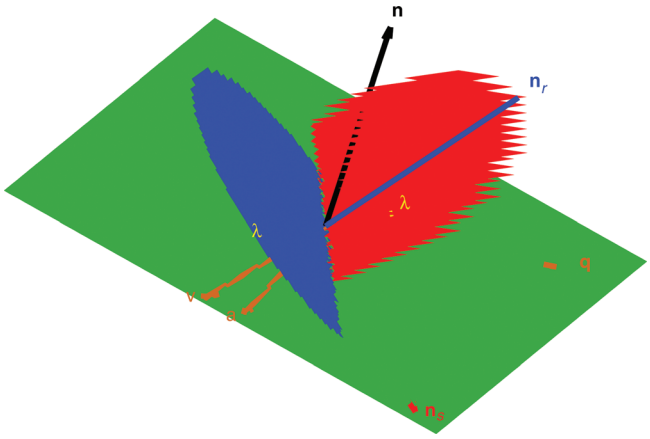


Figure 3. The reflector plane of normal $\mathbf{n}$, together with the source and receiver planes of normals $\mathbf{n}_s$ and $\mathbf{n}_r$, respectively. The figure represents the source/receiver planes displaced with space lag $\boldsymbol{\lambda}$ and time lag τ. The space and time lags are related using equation 17.

So far, we have not assumed any relation between the vectors characterizing the source and receiver planes $\mathbf{n}_s$ and $\mathbf{n}_r$. However, if the source and receiver wavefields correspond to a reflection from a planar interface, these vectors are not independent of one another but are related by Snell's law, which can be formulated as

$$\mathbf{n}_r = \mathbf{n}_s - 2(\mathbf{n}_s \cdot \mathbf{n})\mathbf{n}. \tag{14}$$

This relation follows from geometric considerations and is based on the conservation of ray vector projection along the reflector. Equation 14 is only valid for PP reflections in an isotropic medium.

Substituting Snell's law into system 12–13, and after trivial manipulations of the equations, we obtain the system:

$$[\mathbf{n}_s - (\mathbf{n}_s \cdot \mathbf{n})\mathbf{n}] \cdot \boldsymbol{\lambda} = V\tau, \tag{15}$$

$$(\mathbf{n}_s \cdot \mathbf{n})(\mathbf{n} \cdot \boldsymbol{\lambda}) = 0. \tag{16}$$

In general, the plane characterizing the source wavefield is not orthogonal to the reflection plane (there would be no reflection in that case); therefore, we can simplify equation 16 by dropping the term $(\mathbf{n}_s \cdot \mathbf{n}) \neq 0$. Moreover, in equation 15 we can replace the expression in the square bracket with the quantity $\mathbf{q}\sin\theta$, where $\mathbf{q}$ is the unit vector characterizing the line at the intersection of the reflection and reflector planes and θ is the reflection angle contained in the reflection plane. With these simplifications, system 15–16 can be rewritten as

$$(\mathbf{q} \cdot \boldsymbol{\lambda})\sin\theta = V\tau, \tag{17}$$

$$\mathbf{n} \cdot \boldsymbol{\lambda} = 0. \tag{18}$$

System 17–18 allows for a straightforward physical interpretation of the extended imaging condition. First, expression 18 indicates that of all possible space lags which can be applied to the reconstructed wavefields, the only ones that contribute to the extended image are those for which the space-lag vector $\boldsymbol{\lambda}$ is orthogonal to the reflector normal vector $\mathbf{n}$. Furthermore, assuming that the space shift applied to the source and receiver planes is contained in the reflector plane, i.e., $\boldsymbol{\lambda} \perp \mathbf{n}$, expression 17 describes the moveout function in an extended gather as a function of $\boldsymbol{\lambda}$, τ, θ, and $\mathbf{q}$. The vector $\mathbf{q}$ is orthogonal to the reflector normal and depends on the reflection azimuth angle ϕ.

Figures 1–3 illustrate the process involved in the extended imaging condition and describe pictorially its physical meaning. Figure 1 shows the source and receiver planes as well as the reflector plane together with their unit vector normals. Figure 2 shows the source and receiver planes displaced by $\boldsymbol{\lambda}$ contained in the reflector plane, as indicated by equation 18. The displaced planes do not intersect at the reflection plane; thus, they do not contribute to the extended image at this point. However, with the application of time shifts with the quantity $\tau = (\mathbf{q} \cdot \boldsymbol{\lambda})\sin\theta/V$, i.e., a translation in the direction of plane normals, the source and receiver planes are restored to the image point, contributing to the extended image (Figure 3).

Downloaded 16 May 2011 to 138.67.179.205. Redistribution subject to SEG license or copyright; see Terms of Use at http://segdl.org/

ANGLE DECOMPOSITION

In this section, we discuss the steps required to transform lag-domain CIPs into angle-domain CIPs using the moveout function derived in the preceding section. We also present the algorithm used for angle decomposition and illustrate it using a simple 3D model of a horizontal reflector in a medium with constant velocity that allows us to validate the procedure analytically.

The outer loop of the algorithm is over the CIPs evaluated during migration. The angle decompositions of individual CIPs are independent of one another; therefore, the algorithm is easily parallelizable over the outer loop. At every CIP, we need to access the information about the reflector normal **n** and the local velocity V. The reflector dip information can be extracted from the conventional image, and the velocity is the same as that used for migration.

Prior to angle decomposition, we also need to define a direction relative to which we measure the reflection azimuth. This direction is arbitrary and depends on the application of the angle decomposition. Typically, the azimuth is defined relative to a reference direction (e.g., north). We define this azimuth direction using an arbitrary vector **v**. Using **n**, we can build the projection of the azimuth vector **a** in the reflector plane as

$$\mathbf{a} = (\mathbf{n} \times \mathbf{v}) \times \mathbf{n}. \tag{19}$$

This construction ensures that **a** is contained in the reflector plane (i.e., it is orthogonal on **n**) and that it is coplanar with **n** and **v** (Figure 1). Of course, this construction is just one of the many possible definitions of the azimuth reference. In the following, we measure ϕ relative to **a** and θ relative to the normal to the reflector, given by **n**.

For every azimuth angle ϕ, using **n** and **a**, we can construct the trial vector **q**, which lies at the intersection of the reflector and the reflection planes. We scan over all possible **q**, although only one azimuth corresponds to the reflection from a given shot. This scan ensures that we capture the reflection information from all shots in the survey. Given the reflector normal (the axis of rotation) and the trial azimuth angle ϕ, we can construct the different **q** by applying the rotation matrix

$$Q(\mathbf{n},\phi) = \begin{bmatrix} n_x^2 + \left(n_y^2 + n_z^2\right)\cos\phi & n_x n_y(1-\cos\phi) - n_z\sin\phi & n_x n_z(1-\cos\phi) + n_y\sin\phi \\ n_y n_x(1-\cos\phi) + n_z\sin\phi & n_y^2 + \left(n_z^2 + n_x^2\right)\cos\phi & n_y n_z(1-\cos\phi) - n_x\sin\phi \\ n_z n_x(1-\cos\phi) - n_y\sin\phi & n_z n_y(1-\cos\phi) + n_x\sin\phi & n_z^2 + \left(n_x^2 + n_y^2\right)\cos\phi \end{bmatrix} \tag{20}$$

to **a**, i.e.,

$$\mathbf{q} = Q(\mathbf{n},\phi)\mathbf{a}. \tag{21}$$

In this formulation, the normal vector **n** of components $\{n_x, n_y, n_z\}$ can take arbitrary orientations and does not need to be normalized. Then, for every reflection angle θ, we map the lag-domain CIP gather to the angle domain by summation over the surface defined by equation 17. This operation represents a planar Radon transform (a slant stack) over an analytically defined surface in $\{\lambda, \tau\}$ space. The output is the representation of the CIP gather in the angle domain. To preserve the signal bandwidth, the slant stack needs to use a rho filter, which compensates for the high-frequency decay caused by the summation (Claerbout, 1976). The explicit algorithm for angle decomposition is given in Appendix A.

Next, consider a simple 3D model consisting of a horizontal reflector in a constant-velocity medium. We simulate one shot in the center of the model at coordinates $x = 4$ km and $y = 4$ km, with receivers distributed uniformly on the surface on a grid spaced every 20 m in the x- and y-directions. We use time-domain finite differences for modeling. Figure 4 represents the image obtained by wave-equation migration of the simulated shot using downward continuation. The illumination is limited to a narrow region around the shot because of the limited array aperture.

Figure 5a-d depicts CIP gathers obtained by migrating the simulated shot at the reflector depth and at coordinates $\{x, y\}$ equal to $\{3.2, 3.2\}$ km, $\{3.2, 4.8\}$ km, $\{4.8, 4.8\}$ km, and $\{4.8, 3.2\}$ km, respectively. For these CIP gathers, the reflection angle is invariant $\theta = 48.5°$, but the azimuth angles relative to the x-axis are $-135°$, $+135°$, $+45°$, and $-45°$, respectively. Figure 5e-h shows the angle decomposition in polar coordinates. Here, we use the trigonometric convention to represent ϕ, and we represent the reflection angle in every azimuth in the radial direction (with normal incidence at the center of the plot). Each radial line corresponds to 30°, and each circular contour corresponds to 15°.

Similarly, Figure 6a-d depicts CIP gathers obtained by migrating the simulated shot at the reflector depth and at coordinates $\{x, y\}$ equal to $\{2.8, 2.8\}$ km, $\{3.2, 3.2\}$ km, $\{3.6, 3.6\}$ km, and $\{4.0, 4.0\}$ km, respectively. For these CIP gathers, the azimuth angle is invariant, $\phi = -135°$; but the reflection angles relative to the reflector normal are 59.5°, 48.5°, 29.5°, and 0°, respectively.

In all examples, the decomposition angles correspond to the theoretical values, confirming the validity of our decomposition.

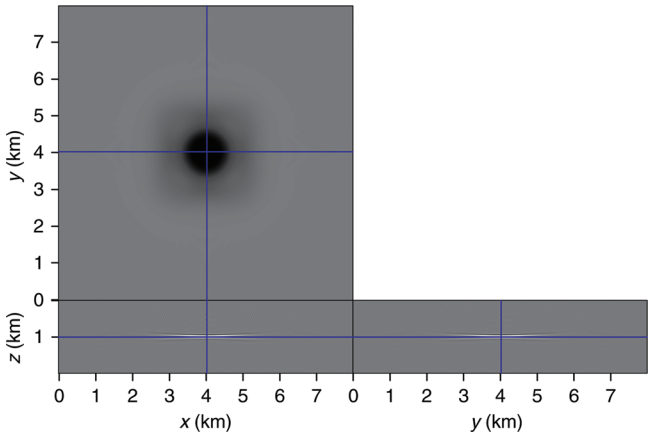


Figure 4. The image obtained for a horizontal reflector in constant velocity using one shot located in the center of the model.

Downloaded 16 May 2011 to 138.67.179.205. Redistribution subject to SEG license or copyright; see Terms of Use at http://segdl.org/

EXAMPLES

We illustrate our method with CIP gathers constructed using wide-azimuth SEG Advanced Modeling Corporation (SEAM) data. Figure 7 shows the velocity model in the area used for imaging, and Figure 8 shows the conventional zero-lag crosscorrelation image. For demonstration, we consider 16 shots whose locations are denoted by the thick dots in Figure 9d. The thin dots represent all 357 shots available in one of the SEAM data subsets. The solid lines in Figure 9a and 9b depict the decimated receiver lines for each of the three shots shown. In all views of Figure 9, the large dot indicates the surface projection of the CIP gathers used for illustration, located at coordinates $\{x, y, z\} = \{23.450, 11.425, 2.38\}$ km. For this example, we consider the azimuth reference vector oriented in the x-direction, i.e., $\mathbf{v} = \{1, 0, 0\}$.

Figure 10a-c shows the extended image obtained at the CIP-gather location indicated earlier using migration by downward continuation. The extended image cubes use 41 grid points in the λ_x and λ_y directions, sampled on the image grid at every 30 m, and 31 grid points in the τ-direction, sampled on the data grid every 8 ms. The vertical lag λ_z is

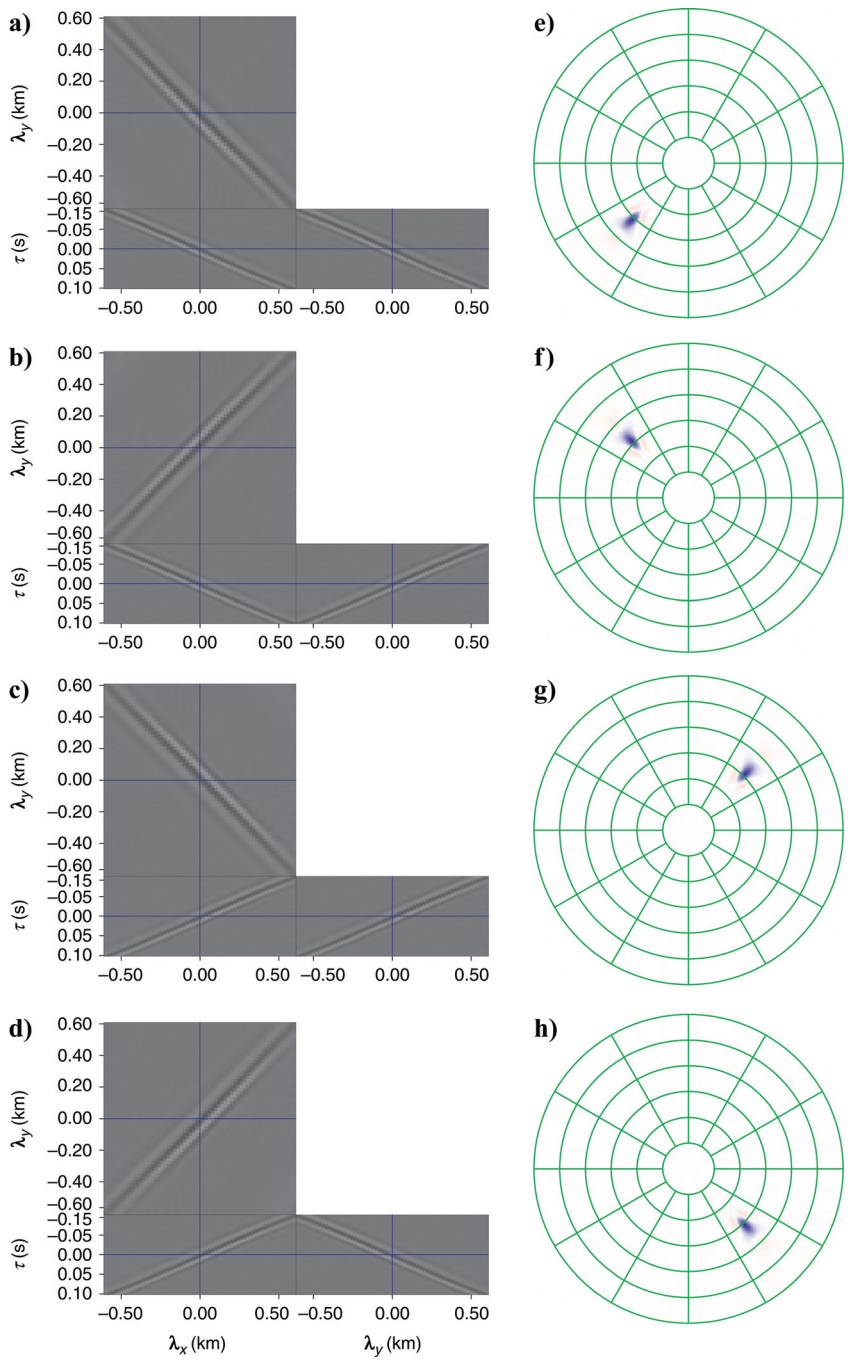


Figure 5. CIP-gather angle decomposition for illumination at a fixed reflection angle. (a-d) Lag-domain CIP gathers. (e-f) Angle-domain CIP gathers in polar coordinates. The angles ϕ and θ are indexed along the contours using the trigonometric convention and along the radial lines, increasing from the center.

Downloaded 16 May 2011 to 138.67.179.205. Redistribution subject to SEG license or copyright; see Terms of Use at http://segdl.org/

not computed in this example because the analyzed reflector is nearly horizontal. This lag is computed in the decomposition process from the horizontal lag and from the known information about the normal to the reflector at the given position. Figure 10d shows the extended image obtained for all 16 shots used for imaging. Although we show the extended image cubes for independent shots, in practice these cubes need not be computed separately — the decomposition separates the information corresponding to different angles of incidence.

Finally, Figure 11 shows the angle-domain decomposition of the extended image cubes shown in Figure 10. In these plots, the circles indicating the reflection angles are drawn every 15°, and the radial lines indicating the azimuth directions are drawn

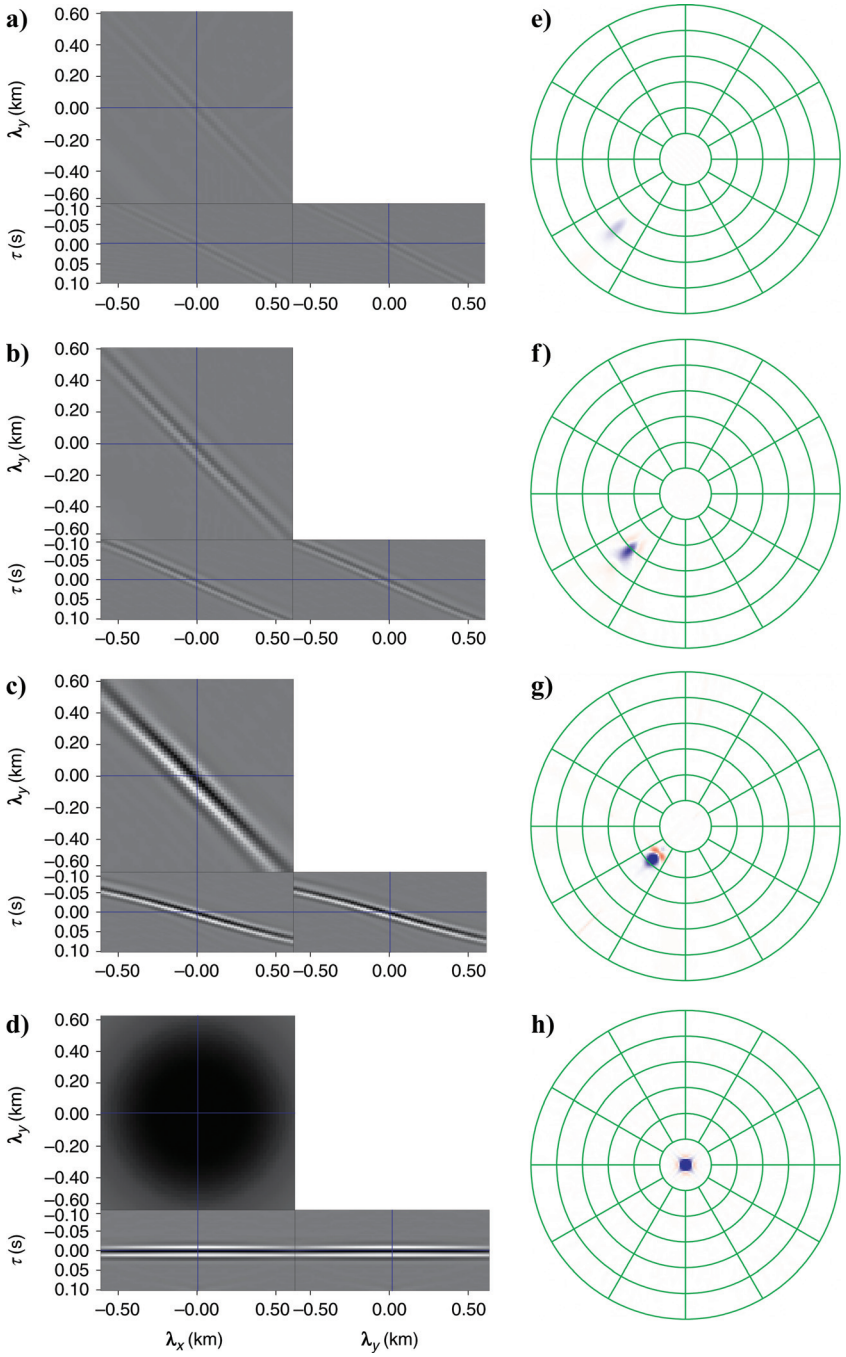


Figure 6. CIP-gather angle decomposition for illumination at a fixed azimuth angle. (a-d) Lag-domain CIP gathers. (e-h) Angle-domain CIP gathers in polar coordinates. The angles ϕ and θ are indexed along the contours using the trigonometric convention and along the radial lines, increasing from the center.

Downloaded 16 May 2011 to 138.67.179.205. Redistribution subject to SEG license or copyright; see Terms of Use at http://segdl.org/

every 15°. Given the sparse shot sampling, the CIP gather is sparsely illuminated but at the correct reflection and azimuth angles.

DISCUSSION

We do not suggest that the wavefields used for imaging are planar prior to interaction with the reflector. In complex geology, such an assumption would be unrealistic. However, a wavefield of arbitrary shape can be thought of as a superposition of plane waves propagating in various directions, either because the wavefronts characterizing the wavefields have curvature or because the wavefields have triplicated during propagation. Each incident plane has a corresponding reflected plane related through Snell's law. Some angle-decomposition techniques explicitly use a planar decomposition of the wavefields, followed by selection through thresholding of the most energetic plane (Xu et al., 2010). In contrast, we rely on the fact that all planar components of the wavefields have been transformed as planar events in the extended images and rely on slant stacks or equivalent methods to separate them as a function of azimuth and reflection angles.

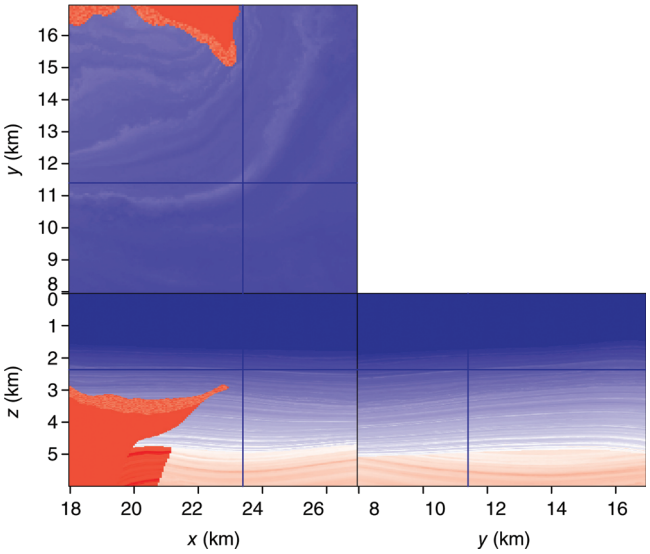


Figure 7. A subset of the SEAM velocity model used for the imaging example in Figures 8–11.

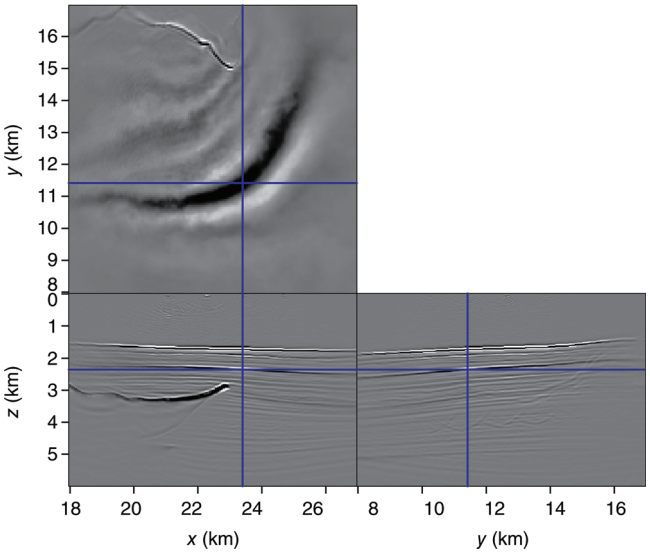


Figure 8. Conventional image obtained using wavefield extrapolation with the 16 shots shown in Figure 9d.

As indicated, we do not need to compute all space lags at the considered CIP-gather positions. We could compute just two of them, e.g., λ_x and λ_y, and then reconstruct the third lag using the information given by the reflector normal at the CIP-gather position (equation 18). If the reflector is nearly vertical, it may be more relevant to compute the vertical lag and one horizontal space lag. Alternatively, we could avoid computing the reflector normal vector from the conventional image and instead compute all three components of the space-lag vector $\boldsymbol{\lambda}$. In this case, as indicated by Sava and Vasconcelos (2011), we could estimate the reflector dip from the lag information prior to angle decomposition.

We have also noted that the relevant space lags are constructed in the reflector plane. This is a direct consequence of the fact that we have considered equal source and receiver wavefields but with opposite sign time shifts. Without this convention, the angle-decomposition problem becomes more complex. In our experience, we did not find the need to relax this requirement.

The angle-domain CIP gathers accurately indicate the sampling of the reflector as a function of azimuth and reflection angles. If the shot distribution is sparse or if the subsurface geology creates shadow zones, the illumination is also sparse. This is beneficial, assuming that the angle-domain CIP gathers are used to evaluate illumination; but it can also be a drawback if the angle-domain CIP gathers are used for AVA or migration velocity analysis (MVA). However, a sparse sampling of a reflector is not a feature of angle decomposition; it is a feature of the acquisition geometry. No angle decomposition can compensate for the lack of adequate data illuminating the subsurface on a dense angular grid.

Finally, the most likely application for angle decomposition in complex geology is the study of reflector illumination. Assuming that the sampling is sufficiently dense and that the imaging velocity is accurately known, we can use the angle decomposition discussed in this paper to evaluate AVA and reflection angles. However, this exercise is relevant only if the reflector illumination is sufficiently dense. Otherwise, AVA effects overlap with illumination effects, rendering the analysis unreliable. Migration velocity analysis in the angle domain may also suffer from the lack of adequate illumination. This partial illumination may deteriorate the moveout that would otherwise be observed in the extended image domain. Furthermore, we do not advocate an implementation of MVA in the angle domain but rather in the extended image domain, which contains all of the relevant information and avoids the additional step of angle decomposition. An extensive discussion of this problem is outside the scope of our paper.

Downloaded 16 May 2011 to 138.67.179.205. Redistribution subject to SEG license or copyright; see Terms of Use at http://segdl.org/

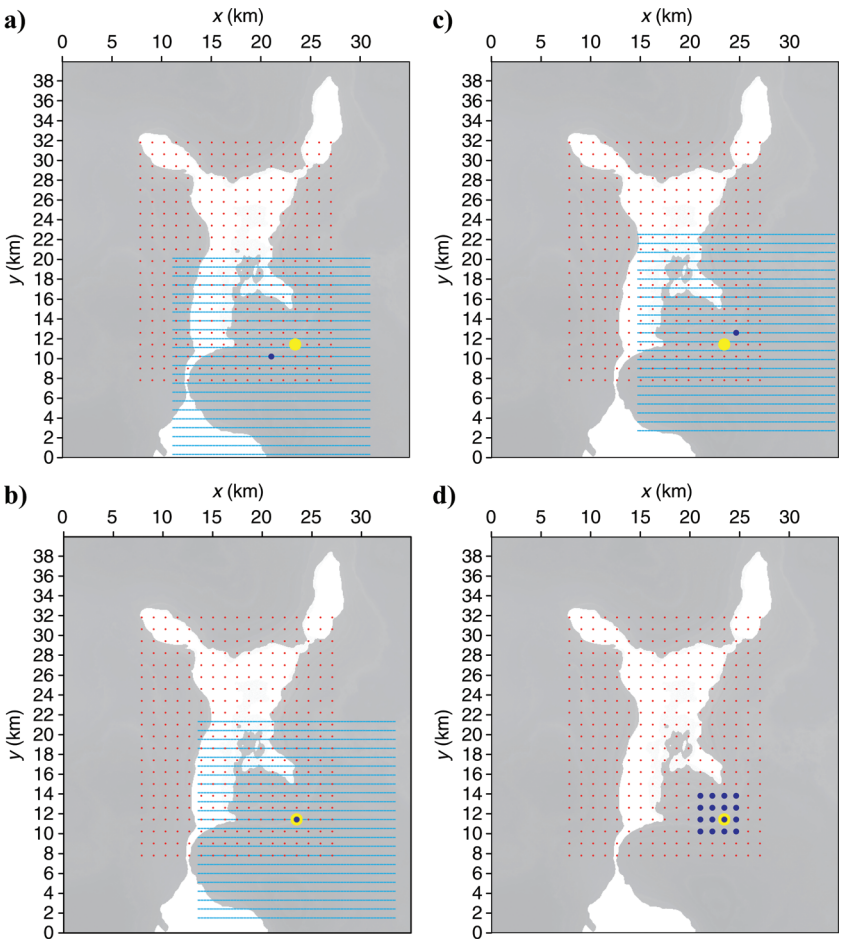


Figure 9. Geometry of SEAM imaging experiment. (a-c) The position of one shot and the associated receiver lines (decimated by a factor of 30 in the *y*-direction. (d) Locations of the 16 shots used for creating the image shown in Figure 8.

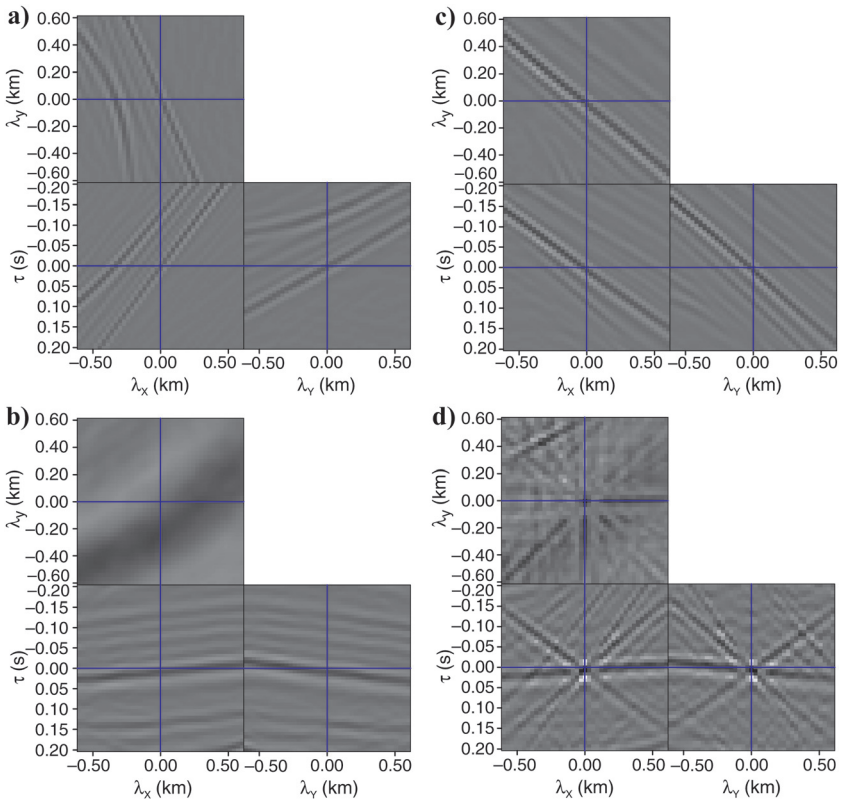


Figure 10. Extended image cubes for the SEAM imaging experiment. (a-c) Extended image cubes at the same location for three different shots. (d) The extended image obtained for all 16 shots considered in this experiment.

Downloaded 16 May 2011 to 138.67.179.205. Redistribution subject to SEG license or copyright; see Terms of Use at http://segdl.org/

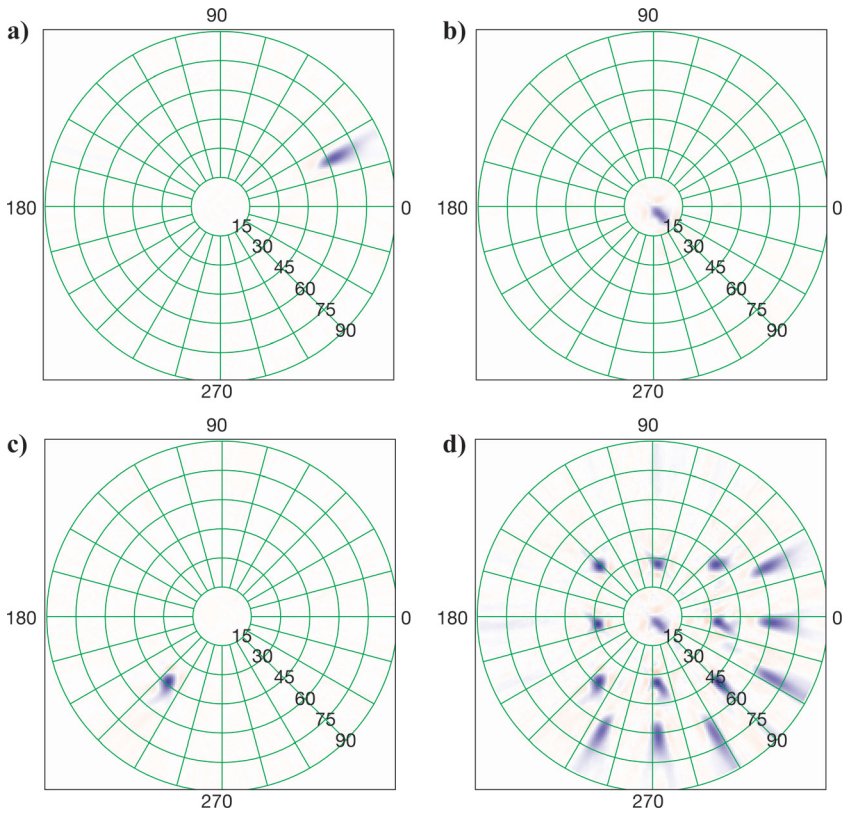


Figure 11. Reflectivity as a function of reflection and azimuth angles for the SEAM imaging experiment. (a-c) The angle-domain CIP gathers at the same location for three different shots. (d) The angle-domain CIP gather obtained for all 16 shots considered in this experiment. The angles ϕ and θ are indexed along the contours using the trigonometric convention and along the radial lines, increasing from the center.

CONCLUSIONS

Angle decomposition based on wavefield-extrapolation methods is characterized by robustness in areas with sharp velocity variation and by accuracy in the presence of steeply dipping reflectors. Extended CIP gathers constructed at discrete image points provide sufficient information for angle decomposition. The decomposition is based on the planar approximation of the source and receiver wavefields in the immediate vicinity of the image points. Space- and time-lag extensions are required to completely characterize the reflection geometry given by the local reflection and azimuth angles. However, assuming that information about the reflector slope is available, we could avoid computing one lag of the extended image, usually the vertical. This increases the computational efficiency of the method and makes it affordable for large-scale, wide-azimuth imaging projects.

ACKNOWLEDGMENTS

P. Sava acknowledges the support of the sponsors of the Center for Wave Phenomena (CWP) at Colorado School of Mines. I. Vlad acknowledges Statoil for support of this research. The reproducible numeric examples in this paper use the Madagascar open-source software package freely available from http://www.reproducibility.org. The wide-azimuth data are the property of SEG Advanced Modeling Corporation (SEAM) and were provided to CWP by ExxonMobil Upstream Research.

APPENDIX A

WIDE-AZIMUTH ANGLE DECOMPOSITION ALGORITHM

This appendix shows the pseudocode used for angle decomposition, indicating the loop order and the link with the theory discussed in the body of the paper.

```
CIP loop                    c = 1...N {
read reflector dip              n
read azimuth reference          v
rotate azimuth reference        {n, v} → a, (equation 19)
read velocity                   V
read CIP                        R(λ, τ)
azimuth angle loop              loop φ = 0°...360° {
rotate by azimuth                   {n, φ, a} → q, (equation 21)
reflection angle loop               loop θ = 0°...90° {
apply slant stack                       R(λ, τ) ⇒ R(φ, θ), (equation 17)
                                    }
                                }
write                           R(φ, θ)
                            }
```

Downloaded 16 May 2011 to 138.67.179.205. Redistribution subject to SEG license or copyright; see Terms of Use at http://segdl.org/

REFERENCES

Berkhout, A. J., 1982, Imaging of acoustic energy by wave field extrapolation: Elsevier Scientific Publ. Co., Inc.

Biondi, B., and P. Sava, 1999, Wave-equation migration velocity analysis: 69th Annual International Meeting, SEG, Expanded Abstracts, 1723–1726.

Biondi, B., and W. Symes, 2004, Angle-domain common-image gathers for migration velocity analysis by wavefield-continuation imaging: Geophysics, **69**, 1283–1298, doi:10.1190/1.1801945.

Biondi, B., and T. Tisserant, 2004, 3D angle-domain common-image gathers for migration velocity analysis: Geophysical Prospecting, **52**, 575–591, doi:10.1111/j.1365-2478.2004.00444.x.

Brandsberg-Dahl, S., M. V. de Hoop, and B. Ursin, 2003, Focusing in dip and AVA compensation on scattering-angle/azimuth common image gathers: Geophysics, **68**, 232–254, doi:10.1190/1.1543210.

Claerbout, J. F., 1976, Fundamentals of geophysical data processing: Blackwell Scientific Publications.

——, 1985 Imaging the earth's interior: Blackwell Scientific Publications.

Clarke, R., G. Xia, N. Kabir, L. Sirgue, and S. Michell, 2006, Case study: A large 3D wide azimuth ocean bottom node survey in deepwater GOM: 76th Annual International Meeting, SEG, Expanded Abstracts, 1128–1132.

Clayton, R. W., and R. H. Stolt, 1981, A Born-WKBJ inversion method for acoustic reflection data: Geophysics, **46**, 1559–1567, doi:10.1190/1.1441162.

de Bruin, C. G. M., C. P. A. Wapenaar, and A. J. Berkhout, 1990, Angle-dependent reflectivity by means of prestack migration: Geophysics, **55**, 1223–1234, doi:10.1190/1.1442938.

Faye, J. P., and J. P. Jeannot, 1986, Prestack migration velocities from focusing depth analysis: 56th Annual International Meeting, SEG, Expanded Abstracts, 483–440.

Gray, S. H., J. Etgen, J. Dellinger, and D. Whitmore, 2001, Seismic migration problems and solutions: Geophysics, **66**, 1622–1640, doi:10.1190/1.1487107.

Koren, Z., I. Ravve, E. Ragoza, A. Bartana, P. Geophysical, and D. Kosloff, 2008, Full-azimuth angle domain imaging: 78th Annual International Meeting, SEG, Expanded Abstracts, 2221–2225.

MacKay, S., and R. Abma, 1992, Imaging and velocity estimation with depth-focusing analysis: Geophysics, **57**, 1608–1622, doi:10.1190/1.1443228.

——, 1993, Depth-focusing analysis using a wavefront-curvature criterion: Geophysics, **58**, 1148–1156, doi:10.1190/1.1443498.

Michell, S., E. Shoshitaishvili, D. Chergotis, J. Sharp, and J. Etgen, 2006, Wide azimuth streamer imaging of Mad Dog: Have we solved the subsalt imaging problem?: 76th Annual International Meeting, SEG, Expanded Abstracts, 2905–2909.

Mosher, C. C., D. J. Foster, and S. Hassanzadeh, 1997, Common angle imaging with offset plane waves: 67th Annual International Meeting, SEG, Expanded Abstracts, 1379–1382.

Nemeth, T., 1995, Velocity estimation using tomographic depth-focusing analysis: 65th Annual International Meeting, SEG, Expanded Abstracts, 465–468.

——, 1996, Relating depth-focusing analysis to migration velocity analysis: 66th Annual International Meeting, SEG, Expanded Abstracts, 463–466.

Prucha, M., B. Biondi, and W. Symes, 1999, Angle-domain common image gathers by wave-equation migration: 69th Annual International Meeting, SEG, Expanded Abstracts, 824–827.

Regone, C., 2006, Using 3D finite-difference modeling to design wide azimuth surveys for improved subsalt imaging: 76th Annual International Meeting, SEG, Expanded Abstracts, 2896–2900.

Rickett, J., and P. Sava, 2002, Offset and angle-domain common image-point gathers for shot-profile migration: Geophysics, **67**, 883–889, doi:10.1190/1.1484531.

Sava, P., and B. Biondi, 2004a, Wave-equation migration velocity analysis — I: Theory: Geophysical Prospecting, **52**, 593–606, doi:10.1111/j.1365-2478.2004.00447.x.

——, 2004b, Wave-equation migration velocity analysis — II: Subsalt imaging examples: Geophysical Prospecting, **52**, 607–623, doi:10.1111/j.1365-2478.2004.00448.x.

Sava, P., and S. Fomel, 2003, Angle-domain common image gathers by wavefield continuation methods: Geophysics, **68**, 1065–1074, doi:10.1190/1.1581078.

——, 2005, Coordinate-independent angle-gathers for wave equation migration: 75th Annual International Meeting, SEG, Expanded Abstracts, 2052–2055.

——, 2006, Time-shift imaging condition in seismic migration: Geophysics, **71**, no. 6, S209–S217, doi:10.1190/1.2338824.

Sava, P., and I. Vasconcelos, 2011, Extended imaging condition for wave-equation migration: Geophysical Prospecting, **59**, 35–55, doi:10.1111/j.1365-2478.2010.00888.x.

Shen, P., and W. W. Symes, 2008, Automatic velocity analysis via shot profile migration: Geophysics, **73**, no. 5, VE49–VE59, doi:10.1190/1.2972021.

Shen, P., W. Symes, and C. C. Stolk, 2003, Differential semblance velocity analysis by wave-equation migration: 73rd Annual International Meeting, SEG, Expanded Abstracts, 2132–2135.

Stolk, C. C., and W. W. Symes, 2004, Kinematic artifacts in prestack depth migration: Geophysics, **69**, 562–575, doi:10.1190/1.1707076.

Stolt, R. H., and A. B. Weglein, 1985, Migration and inversion of seismic data: Geophysics, **50**, 2458–2472, doi:10.1190/1.1441877.

Symes, W., 2008, Migration velocity analysis and waveform inversion: Geophysical Prospecting, **56**, 765–790, doi:10.1111/j.1365-2478.2008.00698.x.

Weglein, A. B., and R. H. Stolt, 1999, Migration-inversion revisited (1999): The Leading Edge, **18**, 950–952, doi:10.1190/1.1438416.

Wu, R.-S., and L. Chen, 2006, Directional illumination analysis using beamlet decomposition and propagation: Geophysics, **71**, no. 4, S147–S159, doi:10.1190/1.2204963.

Xie, X., and R. Wu, 2002, Extracting angle domain information from migrated wavefield: 72nd Annual International Meeting, SEG, Expanded Abstracts, 1360–1363.

Xu, S., H. Chauris, G. Lambare, and M. S. Noble, 1998, Common angle image gather: A new strategy for imaging complex media: 68th Annual International Meeting, SEG, Expanded Abstracts, 1538–1541.

Xu, S., Y. Zhang, and B. Tang, 2010, 3D common image gathers from reverse time migration: 80th Annual International Meeting, SEG, Expanded Abstracts, 3257–3262.

Zhu, X., and R.-S. Wu, 2010, Imaging diffraction points using the local image matrices generated in prestack migration: Geophysics, **75**, no. 1, S1–S9, doi:10.1190/1.3277252.

Downloaded 16 May 2011 to 138.67.179.205. Redistribution subject to SEG license or copyright; see Terms of Use at http://segdl.org/